NANO LETTERS

Letter

pubs.acs.org/NanoLett

Thermal Properties and Phonon Spectral Characterization of Synthetic Boron Phosphide for High Thermal Conductivity Applications

Joon Sang Kang,[†] Huan Wu,[†] and Yongjie Hu*

Department of Mechanical and Aerospace Engineering, University of California, Los Angeles, California 90095, United States

Supporting Information

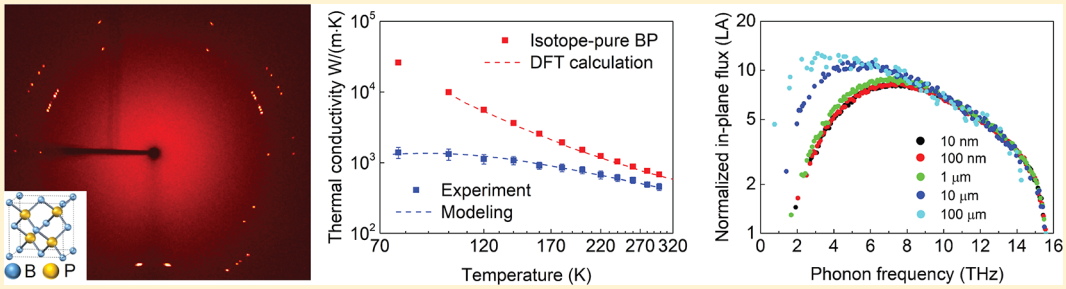

ABSTRACT: Heat dissipation is an increasingly critical technological challenge in modern electronics and photonics as devices continue to shrink to the nanoscale. To address this challenge, high thermal conductivity materials that can efficiently dissipate heat from hot spots and improve device performance are urgently needed. Boron phosphide is a unique high thermal conductivity and refractory material with exceptional chemical inertness, hardness, and high thermal stability, which holds high promises for many practical applications. So far, however, challenges with boron phosphide synthesis and characterization have hampered the understanding of its fundamental properties and potential applications. Here, we describe a systematic thermal transport study based on a synergistic synthesis-experimental-modeling approach: we have chemically synthesized high-quality boron phosphide single crystals and measured their thermal conductivity as a record-high 460 W/mK at room temperature. Through nanoscale ballistic transport, we have, for the first time, mapped the phonon spectra of boron phosphide and experimentally measured its phonon mean free-path spectra with consideration of both natural and isotope-pure abundances. We have also measured the temperature- and size-dependent thermal conductivity and performed corresponding calculations by solving the three-dimensional and spectral-dependent phonon Boltzmann transport equation using the variance-reduced Monte Carlo method. The experimental results are in good agreement with that predicted by multiscale simulations and density functional theory, which together quantify the heat conduction through the phonon mode dependent scattering process. Our finding underscores the promise of boron phosphide as a high thermal conductivity material for a wide range of applications, including thermal management and energy regulation, and provides a detailed, microscopic-level understanding of the phonon spectra and thermal transport mechanisms of boron phosphide. The present study paves the way toward the establishment of a new framework, based on the phonon spectra−material structure relationship, for the rational design of high thermal conductivity materials and nano- to multiscale devices.

KEYWORDS: *Boron phosphide, high thermal conductivity materials, thermal management, heat dissipation, phonon mode, mean free path spectra, ballistic thermal transport, Boltzmann equation, variance-reduced Monte Carlo simulation, ab initio calculations, time-domain thermoreflectance*

With the continuous shrinking of modern electronic and photonic devices, heat dissipation is an increasingly critical technological issue for a broad range of applications encompassing nanoscale transistors, thumbnail-size chips, smart phones, and vehicle electronics as well as data server farms.[1−8] A key challenge and urgent need for effective thermal management is the discovery and development of new high thermal conductivity materials that can effectively dissipate heat from hot spots.[1,2,9] Currently, diamond is the most-developed candidate as a heatsink substrate to enhance cooling efficiency in high-power electronics. However, diamond is far from an optimal candidate given its high cost, slow growth rate, degraded crystal quality, and integration difficulties resulting from high chemical inertness.[10,11] Cubic boron nitride, with its attractive properties, is another candidate benchmark material for thermal management, but production difficulties are a major drawback.[12] Common ways to prepare high-quality cubic boron nitride crystals are borrowed from diamond synthesis and

Received: August 11, 2017
Revised: October 6, 2017
Published: November 8, 2017

DOI: 10.1021/acs.nanolett.7b03437
Nano Lett. 2017, 17, 7507−7514

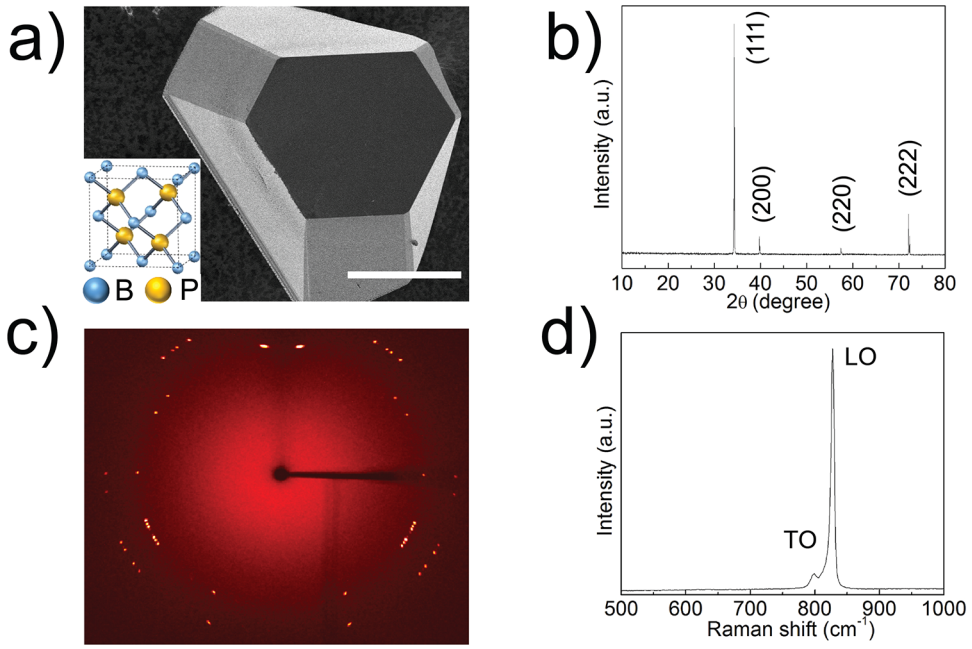

Figure 1. Material synthesis and structural characterization of single-crystal boron phosphide (BP). (a) Scanning electron microscopy image of a sample of BP crystals. The scale bar is 50 μm. The inset schematic illustrates the crystal structure of cubic BP. (b) Powder X-ray diffraction patterns. (c) Single crystal X-ray diffraction image of chemically synthesized BP crystals. (d) Raman spectra of synthetic BP crystals. TO and LO represent the transverse and the longitudinal optical phonon mode, respectively.

require energetic ion-bombardment-assisted methods,[13] high-temperature and high-pressure techniques,[14,15] or epitaxy growth using diamond as a substrate.[16] The lack of easy chemical synthesis routes, along with the issue of suppressing the growth of hexagonal phases, compromise the potential applications of boron nitride. 1D or 2D nanomaterials, such as carbon nanotubes and graphene, are limited by their intrinsic anisotropic thermal conductivity and performance degradation caused by ambient scattering, even though the individual materials offer high thermal conductivities.[9,17]

Presently, the fundamental origin of high thermal conductivity remains unclear. Many recent theoretical works, including first-principles simulations, aim at understanding and developing new high thermal conductivity materials.[18] Among candidate materials, cubic boron phosphide (BP) is an isotropic semiconductor with high thermal conductivity and exceptional chemical refractory properties, high thermal stability, and large elastic modulus as well as a unique potential to be used in nuclear and radiation detectors.[19,20] In addition, in comparison with diamond and cubic boron nitride, the finite semiconductor bandgap of BP provides a flexible control of its electronic properties. Although BP synthesis was first studied in 1957,[21] early studies on BP thermal conductivity are sparse[22,23] and lack detailed descriptions of the structures studied and their measurement characteristics. Understanding the thermal and phonon transport mechanism of BP is critical to appreciating its potential for high thermal conductivity applications. So far, challenges in the synthesis of high-quality crystals[12] and thermal characterization of nanostructures[24] have precluded the experimental investigation of BP as a thermal management candidate. Here, we describe the chemical synthesis of high-quality single BP crystals, the measurement of their temperature- and size-dependent thermal conductivity using ultrafast optical pump probe spectroscopy and the exploration of their phonon spectra through nanoscale ballistic thermal transport. Furthermore, by combining experimental measurements and modeling based on the phonon Boltzmann transport equation and the multiscale variance-reduced Monte Carlo simulation, we determined the intrinsic phonon mean free path spectra of BP and quantified the contribution of the spectral phonon mode dependent scattering to the thermal conductivity of BP. The synergistic experiment-modeling approach presented here may provide insights into a mechanistic understanding of the origin of high thermal conductivity and opens up new opportunities toward the rational design of advanced thermal materials.

Single-crystal BP was synthesized by chemical transport reaction from metal-phosphide solutions through a multistep crystallization process and followed by careful structural characterization to ensure high crystal quality (see the Supporting Information). Figure 1a shows a typical scanning electron microscopy image of the as-synthesized BP crystal. Synthetic BP crystals vary in size from 50 to 500 μm and are mostly hexagonal in shape with the main top crystal surface in the {111} orientation. The crystal morphology of BP is consistent with its crystal structure and growth kinetics: BP is a zinc-blende structure in the $\bar{4}3m$ space group (inset of Figure 1a), where boron and phosphorus atoms with tetrahedral geometry are covalently bonded and form interpenetrating face-centered cubic structures. During BP crystal growth, its {111} crystal orientation has the slowest growth rate as a consequence of the high nucleation energy and usually tends to form the smooth top surface of BP crystals (Figure 1a). This growth restriction results in the stable formation of hexagonally shaped BP crystals bound by {111} plane and allows faster crystal growth in the {110} and {100} directions.[25] The BP single crystal structure was verified by powder X-ray diffraction (P-XRD), single crystal X-ray diffraction (S-XRD), and Raman spectroscopy measurements. P-XRD data show very sharp diffraction peaks of minimum width, which are in agreement

DOI: 10.1021/acs.nanolett.7b03437
Nano Lett. 2017, 17, 7507−7514

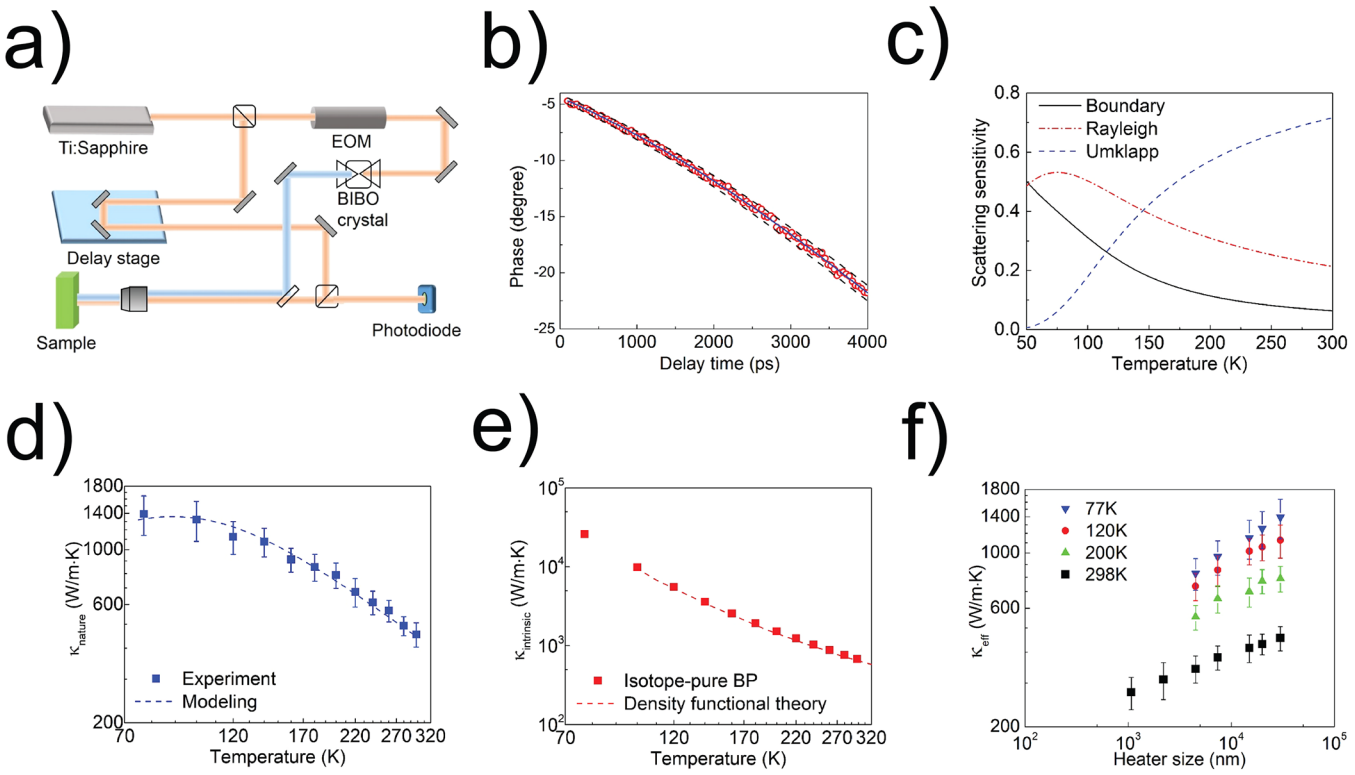

Figure 2. Thermal transport measurements and phonon spectral mapping of boron phosphide (BP). (a) Schematic of ultrafast pump−probe spectroscopy, the time-domain thermoreflectance (TDTR) method used for thermal conductivity measurement. (b) Measurement data and model fitting. Experimental data (red circles) and fits from the multilayer thermal transport model (black line) for the TDTR phase signal. Calculated curves (black dashed lines) using the thermal conductivity changed by ±10% of best values are plotted to illustrate the measurement sensitivity. (c) Scattering sensitivity analysis of different phonon-scattering mechanisms. (d) Measurement data and modeling results of the temperature-dependent thermal conductivity (κ_{nature}) from 77 to 298 K. Experimental data (blue squares) and modeling fit considering multiple phonon scattering processes (dashed blue line). (e) Temperature-dependent thermal conductivity of isotope-pure BP ($\kappa_{intrinsic}$) extracted from experimental data (red squares) compared to that obtained from density functional theory (DFT) calculations (red dashed line, ref 41). (f) Experimental study of ballistic phonon transport consisting of measuring size-dependent effective thermal conductivity (κ_{eff}) at different temperatures.

with the diffractions from different BP crystal planes (Figure 1b). No additional impurity peaks are present in the P-XRD data and energy-dispersive X-ray spectroscopy data (see the Supporting Information). The lattice constant obtained from XRD measurements is 4.54 Å, which is the second smallest among zinc blende III−V materials and indicates strong lattice bonding of BP.[26] The compact structure and light atomic mass of BP leads to a large overlap of atomic orbitals in the crystal, resulting in high crystal stability[27] and very high melting temperature of ∼3000 °C.[19] The single crystallinity was further verified by S-XRD: under X-ray excitation, the BP sample was rotated over 360°, and the diffraction data were collected at every 2° and merged into the same plot. In the merged plots of the S-XRD image (Figure 1c), each diffraction spot appears clearly as a single dot and no distortion (ring shape or blurred spot) is observed, meaning that all diffraction patterns obtained through the whole crystal are consistent, thus confirming that the entire BP sample has perfect single crystallinity and that there are no grain boundaries. For BP, the optical phonons in the nonmetallic zinc-blende structure are triply degenerated because of the cubic symmetricity. Consequently the optical phonon of BP split into two modes: the transverse optical (TO) and the longitudinal optical (LO) phonon modes.[28] The Raman spectroscopy data of the BP crystal sample (Figure 1d) clearly shows the two peaks at 799 and 829 cm^{-1}, corresponding to the TO and LO phonon modes, respectively. In addition, no difference was observed for the structural characterization performed with different crystals, which indicates a very high crystalline quality and uniformity of grown BP crystals.

The thermal properties of single BP crystals were characterized using a time-domain thermoreflectance (TDTR) method, illustrated in Figure 2a (also see the Supporting Information). TDTR is a reliable technique to measure thermal properties of materials[4,24,29−33] and is used to develop novel experimental spectroscopy techniques to study phonon spectra.[4,34] In our setup, a femtosecond Ti/sapphire laser pulse is split between a pump and a probe pulse. The pump pulse generates a sharp temperature rise on the sample surface. The transient temperature decay, due to the heat impulse, is detected by the probe pulse at different delay times controlled with a mechanical delay stage. The full transient decay curve is then fit with a multilayer thermal model to obtain the thermal conductivity (κ).[29,30] It should be noted that TDTR is well-suited to study BP crystals because it requires no physical contact with the sample, and measurements can be performed over micrometer-size sample. In addition, it allows the investigation and quantification of the phonon spectra through nanoscale ballistic transport, as described below. Figure 2b shows experimental data from our TDTR measurements and fittings. We measured a record high thermal conductivity of BP crystals of ∼460 W/m·K at room temperature. This value is exceeding that of common highly conductive metals, such as copper and silver, and is three times higher than that of single-

DOI: 10.1021/acs.nanolett.7b03437
Nano Lett. 2017, 17, 7507−7514

crystal silicon, which underscores the potential of BP for high thermal conductivity applications.

To investigate the high thermal conductivity transport mechanisms of BP, temperature-dependent thermal conductivity (κ_{nature}) of BP crystal samples was measured from 77 to 298 K (Figure 2d). Following the general temperature-dependent trend of single crystals, thermal conductivity of BP increases nonlinearly at low temperature, due to the suppression of phonon scattering. At 77 K, the measured thermal conductivity of our BP samples reaches a high value of ~1400 W/m·K. This temperature-dependent result is directly related to the phonon scattering mechanisms. Fundamentally, the lattice thermal conductivity by kinetic theory[35] is expressed by:

$$\kappa = \frac{1}{3}\sum_{p}\int C(\omega, p)v_g(\omega, p)\Lambda(\omega, p)\mathrm{d}\omega \quad (1)$$

where $C(\omega,p)$ and $\nu_g(\omega,p)$ represent the spectral volumetric specific heat and the group velocity, respectively, for the phonon mode with frequency ω and polarization p. The phonon mean free path (MFP), $\Lambda(\omega,p) = \nu_g(\omega,p) \cdot \tau(\omega,p)$, describes the average distance that a phonon travels between two successive scattering. The total phonon relaxation time $\tau(\omega,p)$ is contributed by the Rayleigh scattering (τ_r) from impurities or isotopes, the Umklapp scattering (τ_a) from an harmonic phonon−phonon scattering, and the boundary scattering (τ_b), following the Matthiessen rule:[36]

$$\tau^{-1} = \tau_r^{-1} + \tau_a^{-1} + \tau_b^{-1} \quad (2)$$

Importantly, the temperature and the frequency dependence vary for different scattering contributions:[37]

$$\tau_r^{-1} = A\omega^4 \quad (3)$$

$$\tau_b^{-1} = \nu_s/L \quad (4)$$

where ν_s is the sound velocity and L is the crystal size. The Umklapp scattering follows the modified Callaway model[38−40] as:

$$\tau_a^{-1} = BT\omega^2 \exp(-C_u/T) \quad (5)$$

The temperature-dependent experimental data can be well fitted using the above phonon relaxation time model, where A, B, and C_u are respective coefficients. Figure 2d shows plots of both experimental and modeling data. To identify the dominant phonon scattering mechanism in BP crystals, we analyzed the sensitivity of thermal conductivity to each scattering contribution and defined the respective scattering sensitivity as:

$$S_i = -\frac{\mathrm{d}(\ln \kappa)}{\mathrm{d}(\ln \tau_i^{-1})} \quad (6)$$

where τ_i^{-1} refers to one of the different phonon scattering rates, as defined in eqs 2−5. The scattering sensitivity analysis in Figure 2c shows that τ_r affects κ most strongly at low temperature (77 K), while τ_a plays the most-significant role at a high temperature (300 K). This result is consistent with our physical understanding of different scattering mechanisms: at low temperature, phonons with long MFP are prone to scattering due to impurities or limited crystal size, whereas the Umklapp scattering becomes more dominant at higher temperatures. Based on our measurements, we derived the limit for intrinsic thermal conductivity of isotope-pure BP ($\kappa_{intrinsic}$) by only considering the Umklapp scattering and eliminating the impurity/isotope scattering. Interestingly, the measured temperature-dependent thermal conductivity of isotope-pure BP is in very good agreement with the calculation using the density functional theory (DFT)[41] (Figure 2e). At 77 K, $\kappa_{intrinsic}$ reaches a very high value of 26000 W/m·K for isotope-pure BP (versus 1400 W/m·K for κ_{nature}), which confirms the presence of very strong Rayleigh scattering from isotope impurities at low temperature.

To quantify the phonon spectral contribution to heat conduction in BP crystals from different phonon modes, we designed an experiment to measure the heating size dependent thermal conductivity by probing nanoscale quasi-ballistic transport.[4] The effective heating size (D) on the BP crystal samples is controlled by varying the laser spot size, which determines a characteristic thermal length to control the heat-transfer regime. In the diffusive limit, i.e., when D is larger than the phonon mean free paths (Λ) of all of the phonon modes, the measured thermal conductivity approaches the bulk value (κ_{bulk}) because all propagating phonons experience enough scattering to reach local thermal equilibrium and the transport can be accurately described using Fourier's law. However, if D is reduced, phonons with $\Lambda(\omega,p) > D$ will not have enough chances to scatter and thus experience ballistic thermal transport, analogously to thermal radiation. Importantly, the heat flux for the ballistic transport is suppressed from that for the diffusive transport, and the deviations provide information about the contribution to thermal conductivity from MFPs of different phonons. The key metric to evaluate ballistic phonon transport and spectral contribution to thermal conductivity is the effective thermal conductivity (κ_{eff}), which is defined following Fourier's law. For smaller heating sizes (D) or increased phonon MFPs (Λ) at lower temperature, a high portion of phonons will have $\Lambda > D$ and experience ballistic transport, therefore leading to a gradual reduction in κ_{eff}.[4,42] Experimentally, κ_{eff} of BP is measured as a function of heating sizes at variable temperature (Figure 2f). Ballistic transport can be clearly observed in the size-dependent measurements. For example, from D = 30 to 4.5 μm, κ_{eff} decreases by 24% at 298 K and by 42% at 77 K. Note that our study also indicates that the BP crystal boundary scattering in small-size samples can actually dominate phonon transport at low temperature when a high portion of the phonon mean free paths are larger than the sample size, which leads to an underestimation of the thermal conductivity, as it will be lower than the intrinsic bulk value of the material.

To quantitatively understand the ballistic phonon transport in BP crystals and interpret our experimental results, we solved the three-dimensional spectral-dependent phonon Boltzmann transport equation (BTE) with the relaxation time approximation given by:

$$\frac{\partial f}{\partial t} + \nu_g \cdot \nabla f = -\frac{f - f_0}{\tau} \quad (7)$$

where f is the phonon distribution function, and f_0 is the equilibrium Bose−Einstein distribution at local temperature. $\nu_g(\omega,p)$ and $\tau(\omega,p)$ are, respectively, the phonon group velocity and the phonon relaxation time at a certain angular frequency ω and a polarization p. However, it should be noted that it is challenging to solve the three-dimensional (3D) spectral-dependent BTE, especially using deterministic methods.

To solve the BTE for the 3D experimental geometry, we calculated the spectral-dependent phonon BTE in the experimental geometry using the Monte Carlo method. In

DOI: 10.1021/acs.nanolett.7b03437
Nano Lett. 2017, 17, 7507−7514

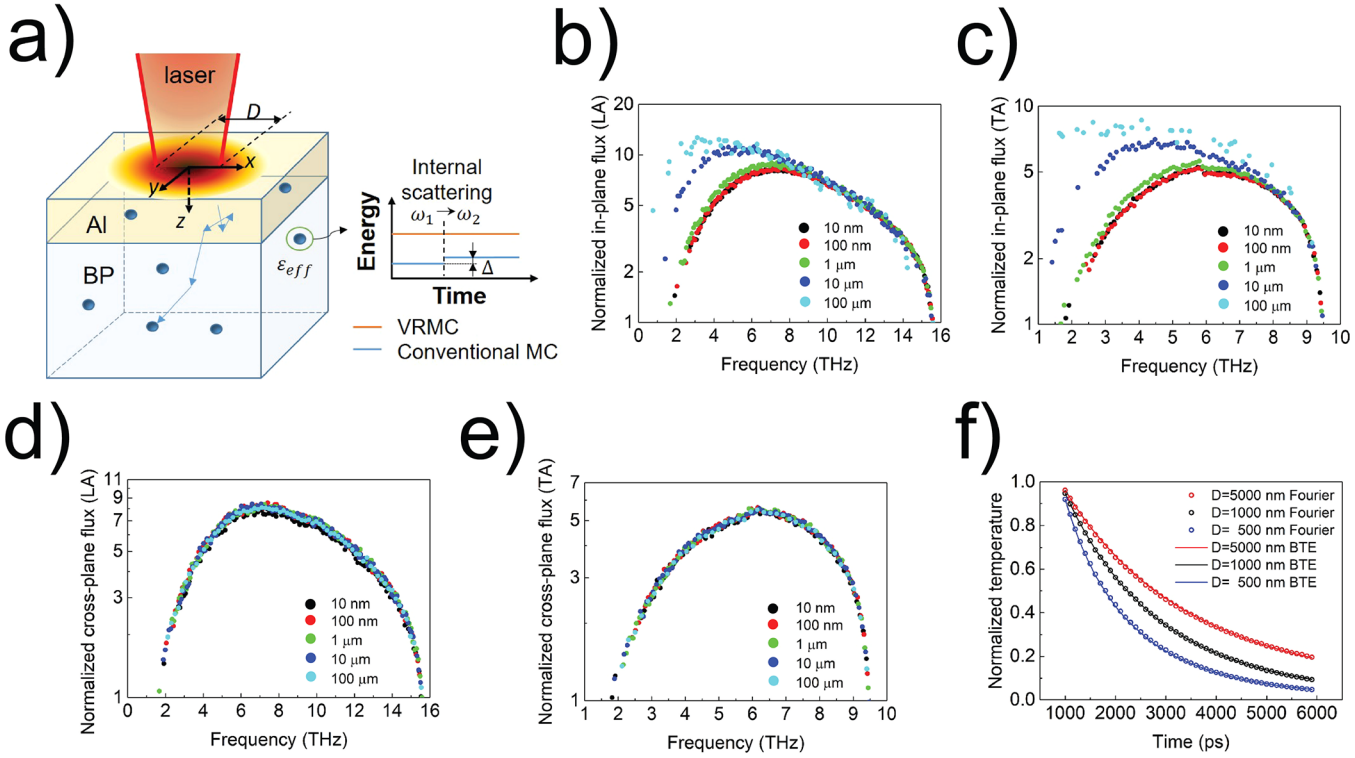

Figure 3. Phonon spectral dependent multiscale simulations based on the Boltzmann transport equation (BTE) and the variance-reduced Monte Carlo (VRMC) method. (a) Schematic of the simulation domain representing the practical experimental geometry. The inset schematic illustrates the comparison between conventional Monte Carlo and VRMC. (b–e) Spectral heat flux contributed from the longitudinal acoustic (LA) and transverse acoustic (TA) phonon modes, respectively, are calculated in the in-plane and cross-plane directions and different heating sizes. (f) Examples of effective thermal conductivity fitting by matching the BTE-calculated temperature decay curve to the Fourier solution at different heating sizes.

the Monte Carlo simulation, a large number of phonon bundles are computed to get a convergent result. Each phonon bundle is processed independently following an "advection–sampling–internal scattering" process, which is repeated until a given simulation time is reached. In the advection procedure, the phonon bundle is moved under the group velocity without internal scattering. In the sampling procedure, the energy of the phonon bundle at a certain position is counted. In the internal scattering procedure, the frequency of the phonon bundle is randomly redistributed. Conventional Monte Carlo simulation has several limitations. First, as illustrated in the inset of Figure 3a, rigorous energy conservation during the phonon internal scattering is challenging because the conventional Monte Carlo simulation conserves the energy by artificially adding or deleting phonon particles until the energy before and after scattering matches within a certain tolerance.[43] However, this method cannot rigidly conserve energy and may cause error in some cases. Second, the conventional Monte Carlo method is time-consuming in the case of small temperature differences due to the need for higher accuracy. Generally in this scenario, a larger quantity of phonon bundles is needed to meet the computational accuracy and ensure that uncertainties are smaller than the finite temperature differences, hence resulting in higher computational costs. Third, the required sampling of the temperature field is also likely to further increase the computational costs. Because the local pseudotemperature is needed to determine the local equilibrium of the Bose–Einstein distribution, a mesh size and time step are required to update the temperature field, which may also lower the accuracy if the mesh size and time step are not small enough.

To enhance the computational accuracy and speed of the simulations, we performed a simulation based on a recently developed variance-reduced Monte Carlo (VRMC) method.[44,45] In this method, the required convergence time is greatly reduced, and the errors introduced by internal scattering are avoided.[44−46] VRMC is most useful in situations with small temperature differences, which is inevitable in TDTR measurements, because the enhanced requirements for computational accuracy at small temperature differences can be easily satisfied without greatly increasing the computation time. The VRMC method solves the deviational energy based on the BTE, as given by:

$$\frac{\partial e^*}{\partial t} + v_g \cdot \nabla e^* = -\frac{e^* - e_0^*}{\tau} \tag{8}$$

where $e^* = e - e_{T_{eq}}^{eq} = \hbar\omega(f - f_{T_{eq}}^{eq})$ is the deviational energy distribution, and $e_0^* = e^{loc} - e_{T_{eq}}^{eq} = \hbar\omega(f_{T_{loc}}^{eq} - f_{T_{eq}}^{eq})$ is the equilibrium deviational energy distribution at local temperature. $\hbar\omega$ is the energy of a single phonon with frequency ω. f is the actual phonon distribution function, and $f_{T_{eq}}^{eq}$ is the Bose–Einstein distribution function at equilibrium temperature T_{eq} = 300 K.

VRMC solves the three challenges of conventional Monte Carlo simulations. First, as we calculate the deviational energy distribution e^* instead of the distribution function f, the energy carried by each phonon bundle is independent from the phonon frequency. Thus, the energy conservation can be rigorously guaranteed during internal scattering,[44] as shown in the inset of Figure 3a. By rigorously following energy

DOI: 10.1021/acs.nanolett.7b03437
Nano Lett. 2017, 17, 7507−7514

conservation during internal scattering, we avoid the uncertain small energy difference before and after internal scattering and consequently enhance the accuracy. For VRMC, there is no need to add or delete phonons in the cell to conserve energy. Second, we only consider the deviational energy from the equilibrium state, which reduces the convergence time, especially in the case of a small temperature difference. VRMC calculates the equilibrium energy deterministically, and only the deviational energy is determined stochastically. The deviational energy is much smaller than the equilibrium energy, particularly in situations of small temperature differences. Given that only a small term of the deviational energy is determined stochastically, the absolute statistical uncertainty is dramatically decreased, thereby greatly reducing the required convergence time.[47] Third, by linearization of the scattering term, each phonon bundles can be simulated independently without the sampling of local pseudotemperatures, and the algorithm requires no integration of time steps and computational cells.[45] Because there is no need to sample in the temperature field, the computational speed is enhanced. Furthermore, because our simulation does not have a mesh and time step, the mesh-induced and time-step-induced inaccuracy is eliminated (see the Supporting Information).

To better understand the anisotropic suppression of the thermal conductivity[48−50] of BP caused by quasi-ballistic phonon transport, we developed detailed phonon spectral flux calculations to analyze the anisotropic heat transfer. We performed phonon spectral dependent simulations to calculate the in- and cross-plane heat flux in BP crystals at different heating sizes. The simulation geometry for the phonon BTE is the same as the experimental condition, in which an Al transducer film on top of the BP sample is heated up by a laser with a circular and Gaussian distributed temperature profile (Figure 3a). During one advection step, the heat flux along a certain direction contributed by a single phonon bundle is proportional to the product of the effective energy of the phonon bundle and the phonon displacement along that direction[45,49] (see the Supporting Information). By cumulating the heat flux contributed by each phonon bundle to the corresponding phonon mode, the heat flux contribution from each phonon mode can be obtained. Figure 3b−e shows the normalized spectral in- and cross-plane heat flux for longitudinal acoustic (LA) and transverse acoustic (TA) phonon polarization. The spectral heat flux in each polarization is normalized by the phonon mode with the smallest MFP, given that the phonon mode with the smallest MFP at the Brillouin zone edge is not suppressed by size confinement. In Figure 3b,c, both polarizations show that the normalized spectral in-plane heat flux is lower when the heating size is smaller, which reveals the heat flux reduction resulting from the size effect. In particular, the low-frequency phonons with long MFPs usually get a large suppression. It is important to note that the in-plane spectral heat flux in Figure 3b,c shows strong dependence on the heating size, whereas the cross-plane spectral heat flux in Figure 3d,e is independent of heating size. Therefore, our detailed phonon spectral flux calculation here conclusively shows that the experimentally measured size-dependent thermal conductivity mainly comes from the in-plane confinement of phonon transport, i.e., lateral ballistic thermal transport takes place for phonon modes with $\Lambda > D$, while the cross-plane heat transfer is not suppressed. The conclusion that anisotropic suppression of thermal conductivity occurs in our TDTR measurements is consistent with recent studies.[48,49]

To make a direct comparison between our experimental TDTR data and the multiscale simulation results calculated with the BTE and VRMC, size-dependent effective thermal conductivity was extracted by matching the temperature decay curve, calculated from the BTE and VRMC results, to the Fourier solution (see the Supporting Information). Figure 3f shows examples of VRMC data and fitting curves for different heating sizes. The surface temperature decays faster with a smaller beam diameter, even though the effective thermal conductivity is smaller, because the larger surface-to-volume ratio of the heating area with a smaller diameter beam increases the heat dissipation efficiency. When plotted together, our TDTR experimental data and our VRMC and BTE calculated results are in good agreement (Figure 4a). This study provides a quantitative analysis based on the BP phonon spectra and shows that the failure of Fourier's law in the ballistic regime is due to in-plane size confinement.

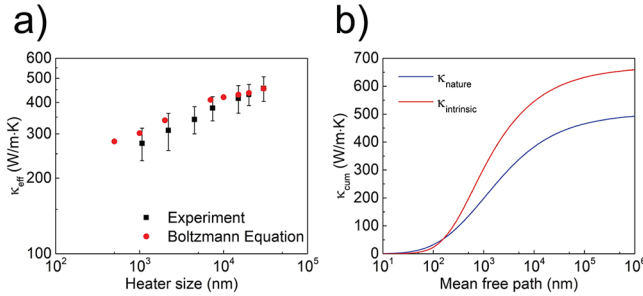

Figure 4. Experimentation and modeling synergy to quantify the ballistic thermal transport and develop the phonon mean free path spectra of boron phosphide (BP). (a) Comparison of the effective size-dependent thermal conductivity (κ_{eff}) predicted with the Boltzmann transport equation (red circles) and experimental measurements (black squares). (b) BP phonon mean free path spectra constructed from measurements: the cumulative thermal conductivity (κ_{cum}) is plotted vs the phonon mean free path for both natural-abundance ($\kappa_{nature,}$ blue line) and isotope-pure BP ($\kappa_{intrinsic,}$ red line).

As a step further, based on our measurements, we constructed the phonon MFP spectra of BP with both naturally abundant (κ_{nature}) and pure isotope ($\kappa_{intrinsic}$) (Figure 4b). The BP phonon MFP spectra was quantified by the cumulative lattice thermal conductivity,[40,51] κ_{cum}, which is defined as the total contribution to thermal conductivity from phonon modes with MFP up to a certain value, Λ':

$$\kappa_{cum}(\Lambda') = \frac{1}{3}\sum_{p}\int_{0}^{\Lambda'} C(\omega, p)v_g(\omega, p)\Lambda(\omega, p)d\omega \quad (9)$$

Without isotope or impurity scattering, the intrinsic bulk thermal conductivity of BP goes up to 681 W/m·K. Interestingly, a crossover between κ_{nature} and $\kappa_{intrinsic}$ is observed for MFP around 100 nm, i.e., $\kappa_{intrinsic}$ is smaller than κ_{nature} for small MFPs, whereas $\kappa_{intrinsic}$ is larger than κ_{nature} for large MFPs. This observation is consistent with our previous measurements of the phonon MFP spectra of silicon and silicon−germanium alloy.[4] Here we attribute the crossover to the fact that Rayleigh scattering, caused by impurities or isotopes, strongly affects high-frequency phonons (see eq 3 above) and further reduces the MFPs of these high-frequency phonons to even smaller values, thereby increasing the contribution from phonon modes

DOI: 10.1021/acs.nanolett.7b03437
Nano Lett. 2017, 17, 7507−7514

with very small MFPs to thermal conductivity. The measured MFP spectra project the phonon spectral contributions of the thermal conductivity into characteristic length scales and are very useful for the direct prediction of thermal transport in more-complex nanostructured materials and devices[40] as well as the development of a rational control of thermal properties.

In summary, we report here for the first time the phonon spectral mapping of BP crystals and the systematic characterization of their thermal transport. High-quality single-crystal BP were chemically synthesized and displayed a record-high room-temperature thermal conductivity of ~460 W/m·K, which is three times higher than that of silicon and exceeds that of the best conducting metals, such as copper and silver. We performed temperature-dependent thermal conductivity measurement using the TDTR technique and analyzed phonon scattering mechanisms through modeling and multiscale simulations. Additionally, we further explored the phonon spectra of BP through quasi-ballistic thermal transport probing and size-dependent measurements. Using the phonon BTE and VRMC simulations, we explain the ballistic transport based on the phonon mode dependent scattering. Furthermore, through a combination of experimentation and modeling, we directly constructed the phonon MFP spectra of BP for both natural-abundance and pure isotopes. These BP spectra are consistent with the density functional theory prediction. Our experimental measurements and modeling analyses of the thermal transport of BP provide a detailed understanding, at the microscopic level, of the phonon spectra of BP and its thermal transport mechanisms. This knowledge is key to the rational design of thermal materials and devices based on the phonon spectra−material structure relationship. BP characteristics unmasked by this study, in association with its unique chemical inertness and refractory behaviors, underscore the promise of BP as an exceptional high thermal conductivity material for a wide range of applications.

■ ASSOCIATED CONTENT

Supporting Information

The Supporting Information is available free of charge on the ACS Publications website at DOI: 10.1021/acs.nanolett.7b03437.

Details of materials chemical synthesis, ultrafast optical spectroscopy, phonon modeling analysis, and multiscale simulation based on the phonon Boltzmann transport equation and the Monte Carlo method. (PDF)

■ AUTHOR INFORMATION

Corresponding Author

*E-mail: yhu@seas.ucla.edu.

ORCID

Yongjie Hu: 0000-0001-7225-1130

Author Contributions

†J.S.K. and H.W. contributed equally to this work.

Notes

The authors declare no competing financial interest.

■ ACKNOWLEDGMENTS

We thank H. Albrecht for careful proofreading of this manuscript. Y.H. acknowledges support from the Young Investigator Award through the U.S. Air Force Office of Scientific Research, the Doctoral New Investigator Award from American Chemical Society Petroleum Research Fund, the UCLA Sustainable LA Grand Challenge, and the Anthony and Jeanne Pritzker Family Foundation.

■ REFERENCES

(1) Waldrop, M. M. *Nature* **2016**, *530* (7589), 144−147.
(2) ITRS. International technology roadmap for semiconductors (ITRS), 2015 ed. http://www.itrs2.net/ (accessed Aug 10th, 2017).
(3) Shehabi, A.; Smith, S.; Sartor, D.; Brown, R.; Herrlin, M.; Koomey, J.; Masanet, E.; Horner, N.; Azevedo, I.; Lintner, W. *United States Data Center Energy Usage Report*; Ernest Orlando Lawrence Berkeley National Laboratory: Berkeley, CA, 2016.
(4) Hu, Y. J.; Zeng, L. P.; Minnich, A. J.; Dresselhaus, M. S.; Chen, G. *Nat. Nanotechnol.* **2015**, *10* (8), 701−706.
(5) Yan, H.; Choe, H. S.; Nam, S. W.; Hu, Y. J.; Das, S.; Klemic, J. F.; Ellenbogen, J. C.; Lieber, C. M. *Nature* **2011**, *470* (7333), 240−244.
(6) Hu, Y. J.; Xiang, J.; Liang, G. C.; Yan, H.; Lieber, C. M. *Nano Lett.* **2008**, *8* (3), 925−930.
(7) Xiang, J.; Lu, W.; Hu, Y. J.; Wu, Y.; Yan, H.; Lieber, C. M. *Nature* **2006**, *441* (7092), 489−493.
(8) Pop, E.; Sinha, S.; Goodson, K. E. *Proc. IEEE* **2006**, *94* (8), 1587−1601.
(9) Balandin, A. A. *Nat. Mater.* **2011**, *10* (8), 569−581.
(10) Won, Y.; Cho, J.; Agonafer, D.; Asheghi, M.; Goodson, K. E. *IEEE Trans. Compon., Packag., Manuf. Technol.* **2015**, *5* (6), 737−744.
(11) Bar-Cohen, A.; Wang, P. On-Chip Thermal Management and Hot-Spot Remediation. In *Nano-Bio- Electronic, Photonic and MEMS Packaging*; Wong, C. P., Moon, K.-S.; Li, Y., Eds.; Springer US: Boston, MA, 2010; pp 349−429.
(12) Rudolph, P. *Handbook of crystal growth: Bulk crystal growth*; Elsevier: Amsterdam, The Netherlands, 2014.
(13) Mirkarimi, P. B.; McCarty, K. F.; Medlin, D. L. *Mater. Sci. Eng., R* **1997**, *21* (2), 47−100.
(14) Mishima, O.; Tanaka, J.; Yamaoka, S.; Fukunaga, O. *Science* **1987**, *238* (4824), 181−183.
(15) Lux, B.; Kalss, W.; Haubner, R.; Taniguchi, T. *Diamond Relat. Mater.* **1999**, *8* (2), 415−422.
(16) Zhang, X. W.; Boyen, H.-G.; Deyneka, N.; Ziemann, P.; Banhart, F.; Schreck, M. *Nat. Mater.* **2003**, *2* (5), 312.
(17) Marconnet, A. M.; Panzer, M. A.; Goodson, K. E. *Rev. Mod. Phys.* **2013**, *85* (3), 1295−1326.
(18) (a) Broido, D. A.; Malorny, M.; Birner, G.; Mingo, N.; Stewart, D. A. *Appl. Phys. Lett.* **2007**, *91* (23), 231922. (b) Mingo, N.; Stewart, D. A.; Broido, D. A.; Srivastava, D. *Phys. Rev. B: Condens. Matter Mater. Phys.* **2008**, *77* (3), 33418. (c) An, J.; Subedi, A.; Singh, D. J. *Solid State Commun.* **2008**, *148* (9), 417−419. (d) Ward, A.; Broido, D. A.; Stewart, D. A.; Deinzer, G. *Phys. Rev. B: Condens. Matter Mater. Phys.* **2009**, *80* (12), 125203. (e) Mingo, N.; Esfarjani, K.; Broido, D. A.; Stewart, D. A. *Phys. Rev. B: Condens. Matter Mater. Phys.* **2010**, *81* (4), 45408. (f) Esfarjani, K.; Chen, G.; Stokes, H. T. *Phys. Rev. B: Condens. Matter Mater. Phys.* **2011**, *84* (8), 85204. (g) Li, W.; Mingo, N.; Lindsay, L.; Broido, D. A.; Stewart, D. A.; Katcho, N. A. *Phys. Rev. B: Condens. Matter Mater. Phys.* **2012**, *85* (19), 195436. (h) Lindsay, L.; Broido, D. A.; Reinecke, T. L. *Phys. Rev. Lett.* **2012**, *109* (9), 95901. (i) Lindsay, L.; Broido, D. A.; Reinecke, T. L. *Phys. Rev. B: Condens. Matter Mater. Phys.* **2013**, *87* (16), 165201. (j) Lindsay, L.; Broido, D. A.; Reinecke, T. L. *Phys. Rev. Lett.* **2013**, *111* (2), 25901. (k) Protik, N. H.; Carrete, J.; Katcho, N. A.; Mingo, N.; Broido, D. *Phys. Rev. B: Condens. Matter Mater. Phys.* **2016**, *94* (4), 45207. (l) Romano, G.; Esfarjani, K.; Strubbe, D. A.; Broido, D.; Kolpak, A. M. *Phys. Rev. B: Condens. Matter Mater. Phys.* **2016**, *93* (3), 35408. (m) Sadasivam, S.; Ye, N.; Feser, J. P.; Charles, J.; Miao, K.; Kubis, T.; Fisher, T. S. *Phys. Rev. B: Condens. Matter Mater. Phys.* **2017**, *95* (8), 85310.
(19) Kumashiro, Y. *J. Mater. Res.* **1990**, *5* (12), 2933−2947.
(20) Lund, J. C.; Olschner, F.; Ahmed, F.; Shah, K. S. *Mater. Res. Soc. Symp. Proc.* **1989**, *162*, 601.
(21) Popper, P.; Ingles, T. A. *Nature* **1957**, *179* (4569), 1075.
(22) Slack, G. A. *J. Phys. Chem. Solids* **1973**, *34* (2), 321−335.

DOI: 10.1021/acs.nanolett.7b03437
Nano Lett. 2017, 17, 7507−7514

(23) Kumashiro, Y.; Mitsuhashi, T.; Okaya, S.; Muta, F.; Koshiro, T.; Takahashi, Y.; Mirabayashi, M. *J. Appl. Phys.* **1989**, *65* (5), 2147−2148.
(24) Cahill, D. G.; Braun, P. V.; Chen, G.; Clarke, D. R.; Fan, S.; Goodson, K. E.; Keblinski, P.; King, W. P.; Mahan, G. D.; Majumdar, A.; Maris, H. J.; Phillpot, S. R.; Pop, E.; Shi, L. *Appl. Phys. Rev.* **2014**, *1* (1), 11305.
(25) Chu, T.; Jackson, J.; Smeltzer, R. *J. Electrochem. Soc.* **1973**, *120* (6), 802−806.
(26) Adachi, S. *Properties of semiconductor alloys: group-IV, III-V and II-VI semiconductors*; John Wiley & Sons: Hoboken, NJ, 2009; Vol. *28*.
(27) Goossens, A.; Schoonman, J. *J. Electrochem. Soc.* **1992**, *139* (3), 893−900.
(28) Sanjurjo, J. A.; Lopez-Cruz, E.; Vogl, P.; Cardona, M. *Phys. Rev. B: Condens. Matter Mater. Phys.* **1983**, *28* (8), 4579−4584.
(29) Schmidt, A. J.; Chen, X.; Chen, G. *Rev. Sci. Instrum.* **2008**, *79* (11), 114902.
(30) Cahill, D. G. *Rev. Sci. Instrum.* **2004**, *75* (12), 5119−5122.
(31) Kang, J. S.; Ke, M.; Hu, Y. *Nano Lett.* **2017**, *17* (3), 1431−1438.
(32) Luckyanova, M. N.; Garg, J.; Esfarjani, K.; Jandl, A.; Bulsara, M. T.; Schmidt, A. J.; Minnich, A. J.; Chen, S.; Dresselhaus, M. S.; Ren, Z.; Fitzgerald, E. A.; Chen, G. *Science* **2012**, *338* (6109), 936−939.
(33) Chiritescu, C.; Cahill, D. G.; Nguyen, N.; Johnson, D.; Bodapati, A.; Keblinski, P.; Zschack, P. *Science* **2007**, *315* (5810), 351−353.
(34) (a) Zeng, L. P.; Collins, K. C.; Hu, Y. J.; Luckyanova, M. N.; Maznev, A. A.; Huberman, S.; Chiloyan, V.; Zhou, J. W.; Huang, X. P.; Nelson, K. A.; Chen, G. *Sci. Rep.* **2015**, *5*, 5. (b) Hoogeboom-Pot, K. M.; Hernandez-Charpak, J. N.; Gu, X.; Frazer, T. D.; Anderson, E. H.; Chao, W.; Falcone, R. W.; Yang, R.; Murnane, M. M.; Kapteyn, H. C.; Nardi, D. *Proc. Natl. Acad. Sci. U. S. A.* **2015**, *112* (16), 4846−4851. (c) Regner, K. T.; Sellan, D. P.; Su, Z.; Amon, C. H.; McGaughey, A. J. H.; Malen, J. A. *Nat. Commun.* **2013**, *4*, 1640. (d) Knight, D. W.; Allegretti, A. M.; Vaske, J. J. *Phys. Rev. Lett.* **2012**, *110* (2), 1154. (e) Minnich, A. J.; Johnson, J. A.; Schmidt, A. J.; Esfarjani, K.; Dresselhaus, M. S.; Nelson, K. A.; Chen, G. *Phys. Rev. Lett.* **2011**, *107* (9), 95901. (f) Siemens, M. E.; Li, Q.; Yang, R.; Nelson, K. A.; Anderson, E. H.; Murnane, M. M.; Kapteyn, H. C. *Nat. Mater.* **2010**, *9* (1), 26−30. (g) Koh, Y. K.; Cahill, D. G. *Phys. Rev. B* 2007, *76* (7).
(35) Ziman, J. M. *Electrons and phonons: the theory of transport phenomena in solids*; Oxford University Press: Oxford, U.K., 1960.
(36) Callaway, J. *Phys. Rev.* **1959**, *113* (4), 1046−1051.
(37) Klemens, P. G. *Proc. Phys. Soc., London, Sect. A* **1955**, *68* (12), 1113−1128.
(38) Slack, G. A.; Galginaitis, S. *Phys. Rev.* **1964**, *133* (1A), A253.
(39) Morelli, D. T.; Heremans, J. P.; Slack, G. A. *Phys. Rev. B: Condens. Matter Mater. Phys.* **2002**, *66* (19), 1953041−1953049.
(40) Yang, F.; Dames, C. *Phys. Rev. B: Condens. Matter Mater. Phys.* **2013**, *87* (3), 35437.
(41) Broido, D. A.; Lindsay, L.; Reinecke, T. L. *Phys. Rev. B: Condens. Matter Mater. Phys.* **2013**, *88* (21), 214303.
(42) Chen, G. *J. Heat Transfer* **1996**, *118* (3), 539−545.
(43) Mazumder, S.; Majumdar, A. *J. Heat Transfer* **2001**, *123* (4), 749−759.
(44) Péraud, J.-P. M.; Hadjiconstantinou, N. G. *Phys. Rev. B: Condens. Matter Mater. Phys.* **2011**, *84* (20), 205331.
(45) Péraud, J.-P. M.; Hadjiconstantinou, N. G. *Appl. Phys. Lett.* **2012**, *101* (15), 153114.
(46) Forghani, M.; Hadjiconstantinou, N. G.; Péraud, J.-P. M. *Phys. Rev. B: Condens. Matter Mater. Phys.* **2016**, *94* (15), 155439.
(47) Baker, L. L.; Hadjiconstantinou, N. G. *Phys. Fluids* **2005**, *17* (5), 51703.
(48) Wilson, R. B.; Cahill, D. G. *Nat. Commun.* **2014**, *5*, 5075.
(49) Ding, D.; Chen, X.; Minnich, A. J. *Appl. Phys. Lett.* **2014**, *104* (14), 143104.
(50) Vermeersch, B.; Mohammed, A. M. S.; Pernot, G.; Koh, Y. R.; Shakouri, A. *Phys. Rev. B: Condens. Matter Mater. Phys.* **2015**, *91* (8), 85203.
(51) Dames, C.; Chen, G. Thermal Conductivity of Nanostructured Thermoelectric Materials. In *Thermoelectrics Handbook: macro to nano*; Rowe, D. M., Eds.; CRC Press: Boca Raton, FL, 2006.

DOI: 10.1021/acs.nanolett.7b03437
Nano Lett. 2017, 17, 7507−7514